

The Tiered Radio Extragalactic Continuum (T-RECS) simulation II: HI emission and continuum-HI cross-correlation.

Anna Bonaldi^{1*}, Philippa Hartley¹, Tommaso Ronconi^{2,3,4}, Gianfranco De Zotti^{5,6}, Matteo Bonato⁷

¹ SKA Organization, Jodrell Bank, Lower Whittington, Macclesfield, SK11 9FT, UK

² SISSA, Via Bonomea 265, 34136 Trieste, Italy

³ INAF - Osservatorio di Astrofisica e Scienza dello Spazio (OAS), Via Gobetti 93/3, I-40127 Bologna, Italy

⁴ CN-HPC: National Centre for HPC, Big Data and Quantum Computing - spoke 3, Italy

⁵ INAF - Osservatorio Astronomico di Padova, Vicolo dell'Osservatorio 5, I-45122 Padova, Italy

⁶ Nicolaus Copernicus Academy, Poland

⁷ INAF - Istituto di Radioastronomia and Italian ALMA Regional Centre, Via Gobetti 101, I-40129, Bologna, Italy

June 23, 2023

ABSTRACT

In this paper we extend the Tiered Radio Extragalactic Continuum Simulation (T-RECS) to include HI emission. The HI T-RECS model is based on the most recent HI mass function estimates, combined with prescriptions to convert HI mass to total integrated HI flux. It further models source size, morphology and kinematics, including rotational velocity and HI line width. The continuum T-RECS model is updated to improve the agreement with deeper number counts available at 150 MHz. The model for star-forming galaxies (SFGs) is also modified according to the most recent indications of a star formation rate (SFR)–radio luminosity relation, which depends primarily on stellar mass rather than redshift. We further introduce prescriptions to associate an HI mass to the T-RECS radio continuum SFG and Active Galactic Nuclei (AGN) populations. This gives us a way to meaningfully associate counterparts between HI and continuum catalogues, thus building HI \times continuum simulated observations. Clustering properties of the sources in both HI and continuum are reproduced by associating the galaxies to dark matter haloes of a cosmological simulation. We deliver a set of mock catalogues, as well as the code to produce them, which can be used for simulating observations and predicting results from radio surveys with existing and forthcoming radio facilities, such as the Square Kilometre Array (SKA).

Key words: radio lines: galaxies, radio continuum: galaxies, galaxies: luminosity function, mass function, large-scale structure of Universe, software: simulations

1 INTRODUCTION

The neutral gas component of galaxies can be traced by the 21-cm “spin-flip” transition of neutral hydrogen (HI), which can be detected over the radio continuum emission at a rest frequency of $\nu_{21\text{cm}} \simeq 1.420$ GHz (Hellwig et al. 1970).

So far, due to the faintness of the signal, most untargeted HI observations have observed the local Universe (e.g. HIPASS, Barnes et al. 2001, Wong et al. 2006, ALFALFA Giovanelli et al. 2005; Haynes et al. 2018), with a few targeted fields to extend to slightly higher redshifts (AUDS Xi et al. 2021, BUDHIES Gogate et al. 2023). A new gener-

ation of facilities is allowing HI surveys that will greatly improve over their predecessors in terms of redshift range, survey area, sensitivity and spatial resolution: CHILES on the Jansky Very Large Array (JVLA, Fernández et al. 2016), WALLABY and DINGO on the Australian SKA Pathfinder (ASKAP, Koribalski et al. 2020; Meyer 2009), LADUMA and MIGHTEE on the SKA Precursor MeerKAT (Blyth et al. 2016; Maddox et al. 2021; Ponomareva et al. 2023) and the Apertif imaging surveys (Adams et al. 2022). These observational efforts will culminate with the Square Kilometre Array Observatory (SKAO) planned HI observations (Staveley-Smith & Oosterloo 2015).

Interstellar gas and stars, and the link between them, are at the heart of galaxy formation and galaxy evolution

* E-mail: anna.bonaldi@skao.int

studies. They together account for the galaxy’s baryonic content, and the former fuels the latter through bursts of star-formation activity. In this context, HI and continuum surveys combined are a particularly powerful tool, with the former tracing neutral gas and the latter tracing star formation (e.g. Maddox et al. 2016). In Bonaldi et al. (2019) (hereafter, T-RECS I) we delivered a code, T-RECS¹, to produce mock radio continuum catalogues consistent with the most recent data and models, with the aim of predicting what upcoming and future radio continuum surveys could look like, and to optimise survey specifications to science goals. This work extends its scope to HI surveys, as well as continuum–HI combined studies.

One way to produce mock HI catalogues would be to add HI properties to the radio continuum modelling presented in T-RECS I. However, this would produce catalogues selected in radio continuum rather than HI, which would not be adequate to simulate the untargeted HI surveys mentioned above. In light of this, we have implemented two independent modules: one producing catalogues selected in HI (described in Sec. 2) and one producing catalogues selected in radio continuum (updated from T-RECS I as described in Sec. 3). As a further step, those two outputs can be combined in a consistent HI \times continuum catalogue set as detailed in Sec. 4. This approach explicitly allows for sources in one catalogue either to have or not have a counterpart in the other, based on expected correlations between HI and radio continuum properties and on the respective selection functions. It also gives the option to produce either of the two simulations as stand-alone. This code architecture also easily supports extending to other wavelengths in the future (e.g. optical, infra-red). The issue of including realistic clustering into the simulation is discussed in Sec 5. Finally we draw our conclusions in Sec 6.

In this work, $H_0 = 67$, $\Omega_m = 0.32$, $\Omega_\Lambda = 0.68$, which are the Planck Collaboration VI (2020) Λ CDM best-fit parameters rounded to two significant figures.

2 HI MODEL

2.1 HI flux

Following Duffy et al. (2012), the total integrated HI flux of a source, f_{HI} , can be directly linked to the neutral hydrogen mass, M_{HI} . By adopting an optically-thin approximation for the HI, where self-absorption is negligible, they obtain

$$f_{\text{HI}} = \frac{M_{\text{HI}}}{49.8} d_L^{-2} \text{ Jy Hz} \quad (1)$$

where d_L is the luminosity distance of the source in Mpc and M_{HI} is the HI mass in units of M_\odot . This relation essentially converts between HI luminosity function and HI mass function and it is yet another example of the intrinsic power of HI observations for probing galaxy physics.

To generate T-RECS HI catalogues, we combined this relation with the best-fit $z = 0$ mass function from Jones et al. (2018):

$$\Phi(M_{\text{HI}}) = \ln(10)\phi_*(M_{\text{HI}}/M_{\text{HI}}^*)^{(\alpha+1)} \exp[-M_{\text{HI}}/M_{\text{HI}}^*], \quad (2)$$

¹ <https://github.com/abonaldi/TRECS.git>

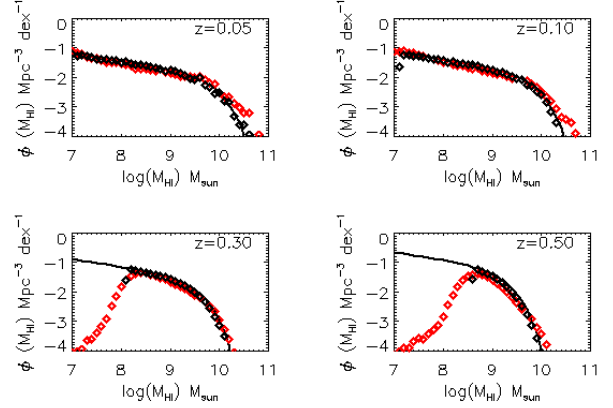


Figure 1. HI mass function from Jones et al. (2018) with redshift evolution constrained by Paul et al. (2023, back lines), compared to the distribution of T-RECS HI masses for an HI catalogue of 25 deg², and flux limit $f_{\text{HI}} = 1 \text{ Jy Hz}$ (black symbols). In red we also show the distribution of the HI mass proxy obtained for a companion continuum simulation of 25 deg², $f_{1.4\text{GHz}} \geq 100 \text{ nJy}$ (see sec. 3.4).

with $\log(M_{\text{HI}}^*) = 9.94 M_\odot$, $\phi_* = 4.5 \times 10^{-3}$, $\alpha = -1.25$.

The redshift evolution of the HIMF is currently poorly constrained by the data, a situation that should drastically improve once the new-generation surveys are completed.

Bera et al. (2022) and Paul et al. (2023) investigated the HIMF at $z \sim 0.3$ with GMRT and MeerKAT data, respectively. They both found a significant evolution of both M_{HI}^* and ϕ_* , which results in far fewer massive HI galaxies at $z = 0.3$ than at $z = 0$.

In line with those results, we parameterize the evolution as

$$\log(M_{\text{HI}}^*(z)) = \log(M_{\text{HI}}^*)_{z=0} + C_{\text{evol}} \times z. \quad (3)$$

$$\log \phi_*(z) = \log \phi_{*z=0} + \phi_{\text{evol}} \times z. \quad (4)$$

We determine the parameters $C_{\text{evol}} = -1.41$, $\phi_{\text{evol}} = 1.55$, by imposing that, at $z = 0.32$, $\log(M_{\text{HI}}^*/M_\odot) = 9.49$ and $\phi_* = 1.4 \times 10^{-2} \text{ Mpc}^{-3} \text{ dex}^{-1}$, which are the best-fit values of Paul et al. (2023).

Given the lack of data on the HIMF at higher redshifts, we restrict the redshift range of the simulation to $z = 0-0.5$, which sets the frequency range for HI surveys we can simulate to 1420.40–946.9 MHz. Fig.1 shows the adopted HI mass function (black line) compared with a T-RECS realization (black symbols) for different redshifts.

2.2 Source size and morphology

There is a tight relation between HI mass and the diameter of the HI disk D_{HI} in kpc, defined at an HI surface density Σ_{HI} of $1 M_\odot \text{ pc}^{-2}$ (e.g., Broeils & Rhee 1997; Verheijen & Sancisi 2001; Swaters et al. 2002; Noordermeer et al. 2005; Wang et al. 2014; Ponomareva et al. 2016; Naluminsa et al. 2021), which appears to be independent of redshift in the so far explored range (Rajohnson et al. 2022). We adopt the recent relation by Naluminsa et al. (2021):

$$\log M_{\text{HI}} = (1.95 \pm 0.03) \log D_{\text{HI}} + (6.5 \pm 0.04), \quad (5)$$

which was derived by using a complete sample of 228 WHISP galaxies including all morphological types. This relation is in particularly good agreement with Broeils & Rhee (1997) and Wang et al. (2016), which have a similar morphological selection. It is steeper than Verheijen & Sancisi (2001); Swaters et al. (2002); Noordermeer et al. (2005), which focused on specific morphological types.

D_{HI} , obtained by inverting eq. (5), is finally converted from the physical size in kpc to an angular size in arcsec depending on the angular diameter distance of the source. For consistency with the continuum module, where the size of SFGs is in terms of a scale radius, the T-RECS catalogue contains the radius $R_{\text{HI}} = D_{\text{HI}}/2$. To further complete the morphological description of the HI sources, the catalogue contains galaxy inclination i which, in the hypothesis of a random orientation, follows a $\sin(i)$ distribution.

Following e.g. Holmberg (1958), galaxy inclination is linked to the axis ratio b/a

$$\cos^2 i = \frac{(b/a)^2 - \kappa^2}{1 - \kappa^2} \quad (6)$$

where κ is the ratio of smallest to largest axis of an oblate spheroid which best represents the galaxy’s 3-dimensional shape. Early measurements indicated values of $k = 0.2$ for spirals and $k = 0.5$ for ellipticals. Rodríguez & Padilla (2013) derive updated distributions for κ by studying the Sloan Digital Sky Survey (SDSS) Galaxy Zoo objects. A Gaussian fit to these distributions yields $\kappa = 0.267 \pm 0.102$ for spirals and $\kappa = 0.438 \pm 0.196$ for ellipticals. We use the previous relations and the galaxy’s size and inclination to derive major and minor axes. Since HI-rich galaxies are predominantly of spiral morphology, we adopt for the whole HI sample the spiral distribution of Rodríguez & Padilla (2013).

2.3 Source HI line width

The width of the 21-cm emission line of neutral hydrogen is related to the circular velocity, corrected for the galaxy’s inclination, by

$$w_{50} = 2 \sin(i) v_{\text{max}} \quad (7)$$

(e.g. Oman 2022), where w_{50} is the full width at half maximum (FWHM) of the 21 cm line and v_{max} is the maximum circular velocity.

Katz et al. (2019) derive empirical scaling relations of v_{max} with the galaxy’s baryonic mass M_{b} (Baryonic Tully-Fisher relation, BTFR), as well as dark matter halo mass, M_{h} , from 120 late-type galaxies from the SPARCS database. We use their BTFR results obtained by using a “flat” prior on the mass-to-light ratio, to derive v_{max} from the baryonic mass. The latter has been modelled as $M_{\text{b}} = M_{\text{HI}} + M_{\text{star}} + M_{\text{H}_2} + M_{\text{HII}}$, where M_{star} is the stellar mass, M_{H_2} is the mass of molecular hydrogen and M_{HII} is the mass of ionised hydrogen. Although there are other baryonic components, the list above contains the majority of baryons in a galaxy.

For M_{star} we use the maximum likelihood $M_{\text{star}}-M_{\text{HI}}$ relation by Naluminsa et al. (2021). Walter et al. (2020) investigate the density of atomic and molecular hydrogen, $\rho_{\text{HI}}(z)$ and $\rho_{\text{H}_2}(z)$, in galaxies as a function of redshift. For M_{H_2} we use $M_{\text{H}_2} = M_{\text{HI}} \rho_{\text{H}_2}(z)/\rho_{\text{HI}}(z)$ where $\rho_{\text{H}_2}(z)$ and $\rho_{\text{HI}}(z)$ are the best-fit relations of Walter et al. (2020) (their table

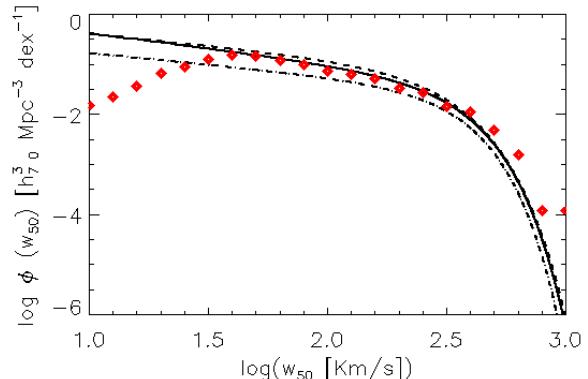


Figure 2. Black lines: HIWF from Oman (2022) computed from the $\alpha.100$ catalogue (solid, dashed and dot-dashed lines are for the “complete”, “spring” and “fall” sky areas, respectively). Red symbols: T-RECS HIWF computed on an HI catalogue of 25 deg^2 , and flux limit $f_{\text{HI}} = 1 \text{ Jy Hz}$, over the 0–0.075 redshift range.

1). For M_{HII} we use the $\log(M_{\text{star}})-\log(M_{\text{HII}}/M_{\text{star}})$ relation by Popping et al. (2014) (linear fit to their Figure 2). This relation is provided in the $\log M_{\text{star}} = 6 - 13 \log M_{\odot}$ and implies an increase of the ionised hydrogen with decreasing stellar mass. To avoid M_{HII} to become unrealistically high for low values of M_{star} , we cap the maximum value of M_{HII} to M_{HI} . Once v_{max} has been obtained, by using the $M_{\text{h}}-v_{\text{max}}$ relation by Katz et al. (2019) we add the modelling of the dark matter mass from HI properties, $M_{\text{h,HI}}$, which is used to model source clustering in Sec 5.

In Fig. 2 we compare the distribution of the T-RECS w_{50} at low redshifts (red symbols) with the HI velocity width function (HIWF) derived from the ALFALFA survey by Oman (2022; black lines). Despite the relative simplicity of the model, there is a good agreement between the two. The decreasing number of T-RECS objects below $w_{50} \sim 10^2$ is due to the catalogues becoming increasingly incomplete. When including higher redshifts, the T-RECS HIWF slowly shifts to lower w_{50} values and increases in amplitude due to the evolution of the HI mass function. We note that our modelling of the line width relies on the presence of a plateau in the velocity curve for $v = v_{\text{flat}}$. This is not representative of irregular or dwarf galaxies (Swaters et al. 2009; Oh et al. 2015) whose measured velocity width would be smaller.

3 RADIO CONTINUUM MODEL

The radio continuum model is described in detail in T-RECS I; here we give a summary and introduce a few modifications. T-RECS models radio continuum sources as either star-forming galaxies (SFGs) or Radio Loud Active Galactic Nuclei (RL AGN). There is no explicit modelling of radio-quiet (RQ) AGN (e.g., Kellermann et al. 2016; Padovani et al. 2015; Mancuso et al. 2017; White et al. 2017; Hartley et al. 2019). RQ AGN can be modelled as objects where star formation in the host galaxy is responsible for the radio emission. On the other hand, observations have also shown that the active nucleus can produce the radio emission. RQ AGN would contribute part of the flux of those sources that, in T-RECS, are modelled as SFGs.

3.1 Star-forming galaxies (SFGs)

SFGs are modelled as in Mancuso et al. (2015) as late-type, spheroidals and lensed spheroidals. The radio emission is based on redshift-dependent star-formation rate (SFR) functions and a modelling of synchrotron, free-free and thermal dust emission as a function of SFR for each of the three sub-populations. The free-free emission and the thermal dust emission are still modelled as in T-RECS I. The synchrotron emission, which is overall the dominant component, is updated in this work to follow the most recent results.

Across the 150 MHz–20 GHz frequency range, we adopt

$$L_{\text{synch}}(\nu) = L(\text{SFR}) \left(\frac{\nu}{\nu_0} \right)^{\alpha + \delta\alpha \log(\nu/\nu_0)}, \quad (8)$$

where $L(\text{SFR})$ follows Smith et al. (2021)

$$\frac{L(\text{SFR})}{\text{W/Hz}} = L_0 \left(\frac{\text{SFR}}{M_\odot/\text{yr}} \right)^\beta \left(\frac{M_{\text{star}}}{10^{10} M_\odot} \right)^\gamma. \quad (9)$$

The frequency dependence is a power-law with spectral index that progressively steepens towards higher frequencies; the parameters are $\alpha = -0.85$, $\delta\alpha = -0.1$, $\nu_0 = 1.6$ GHz. The previous relation we adopted, as in Mancuso et al. (2015), already had a steepening towards the highest frequencies. The most recent data at 150 MHz (Siewert et al. 2019; Mandal et al. 2021) indicate that this behaviour should be extended to the whole frequency range. A possible mechanism for a steepening synchrotron spectral index is synchrotron ageing.

M_{star} in eq. (9) is the stellar mass of the galaxy. This is modelled starting from the SFR using the best-fit SFR– M_{star} relation of Aversa et al. (2015) (their table 2, with redshift evolution). The redshift evolution of M_{star} induces a redshift evolution on the radio luminosity function. Parameters in eq. (9) are $\beta = 0.850 \pm 0.005$, $\gamma = 0.402 \pm 0.005$ (Smith et al. 2021) and $\log(L_0/[\text{WHz}^{-1}]) = 21.28$. The latter differs from the Smith et al. (2021) value of $\log L_0/[\text{W/Hz}] = 22.10$, however our normalization is linked to that of eq. (8) at 150 MHz $\log(L_{\text{sync}}(150\text{MHz})/\log(\text{SFR})) = 0.77$, which needs a $d \log L_0 = -0.77$ correction. Once this is accounted for, there is still a difference in the overall normalization of $d \log L_0 = -0.06$, W/Hz. Given that $L(\text{SFR})$ depends on both SFR and M_{star} as per eq. (9), differences in the distribution of either quantities between the measurements by Smith et al. (2021) and the models in Mancuso et al. (2015) and Aversa et al. (2015) could cause some discrepancy. Furthermore, the parameters we adopt have been chosen to achieve consistency with the available data over the whole 150 MHz–20 GHz range rather than being optimised at 150 MHz.

In Fig. 3 we verify that the updated luminosity functions at 1.4 GHz are in good agreement with the data. The updated comparison of differential source counts in the 150 MHz–20 GHz range is presented in Fig. 4.

As in T-RECS I, the size and shape of SFGs is modelled in terms of elliptical Sersic profiles. As a refinement, we link galaxy inclination to galaxy ellipticity using again eq. (6) with $\kappa = 0.267 \pm 0.102$ for spirals and $\kappa = 0.438 \pm 0.196$ for ellipticals. We make a direct association with the T-RECS radio continuum sub-populations as follows: late-type to spirals, spheroids and lensed spheroids to ellipticals (Rodríguez & Padilla 2013).

3.2 Radio Loud (RL) AGN

RL AGN are based on the Massardi et al. (2010) evolutionary model as updated by Bonato et al. (2017). This model classifies the AGN into steep-spectrum sources (SS-AGN), flat-spectrum radio quasars (FSRQs) and BL Lacs, with different evolutionary properties.

The basis of our AGN model is given by luminosity functions at 1.4 GHz for these populations and for redshift intervals ranging from $z = 0$ to $z = 8$. These trivially translate to flux density at 1.4 GHz given the redshift of the source and the adopted cosmology.

To compute flux densities at other frequencies, Bonato et al. (2017) adopt power-law spectra $S \propto \nu^\alpha$ with $\alpha_{\text{FSRQ}} = \alpha_{\text{BL Lac}} = -0.1$, and $\alpha_{\text{steep}} = -0.8$. T-RECS I modified this simple recipe by allowing for a scatter in the spectral index between different sources. Moreover, it introduced systematic variations with frequency of the spectral index distributions, in order to achieve agreement with multi-frequency observations.

An effective spectral index between the frequencies ν_1 and ν_2 of sources of a given population with flux density S_1 , within dS_1 , at ν_1 , was computed by finding the flux density S_2 at ν_2 such that $N_1(S_1)dS_1 = N_2(S_2)dS_2$. Thus $\alpha_{\text{eff}}(\nu_1, \nu_2)$ is the single spectral index relating the counts at ν_1 to those at ν_2 . This procedure was applied to the 1.4–4.8 GHz and 4.8–20 GHz range, using the Massardi et al. (2010) model up to 5 GHz and the De Zotti et al. (2005) model at higher frequencies. In this work, we extend this approach to the 150 MHz–1.4 GHz frequency range, where we had previously applied the Bonato et al. (2017) indices plus scatter, in order to improve the agreement with the Siewert et al. (2019) and Mandal et al. (2021) counts at 150 MHz.

The morphological model for RL AGN is the same as in T-RECS I. Following the unified model of AGN, we assume the same parent population for all our AGN classes. Intrinsic sizes are drawn using DiPompeo et al. (2013); BL-Lac and FSRQ are then assigned a small viewing angle ($\theta \leq 5$ deg) and SS-AGN a large viewing angle ($5 < \theta \leq 90$ deg), thus creating the familiar dichotomy in observed source sizes. For SS-AGN, the description is completed by Fanaroff & Riley (1974)’s R_s parameter, modelled following Lin et al. (2010), to provide the FRI/FRII classification.

For consistency with the SFG catalogue, we complement the morphological description of AGN with an elliptical/spiral classification of their host galaxy. The issue of radio vs optical morphology was investigated by Kozieł-Wierzbowska et al. (2020) on a sample of 32,616 spectroscopically-selected galaxies from SDSS with radio counterpart from FIRST and VLASS. For our AGN, we adopt their result on galaxies with extended radio morphology, which have an elliptical host in 98 % of cases.

3.3 Dark matter mass modelling from radio continuum properties

As in T-RECS I, we include an estimate of the dark matter (DM) mass of galaxies based on radio continuum properties $M_{\text{h,cont}}$. The main use of this mass is to simulate the clustering properties for our sources. Special attention has been given to ensuring that the obtained T-RECS DM

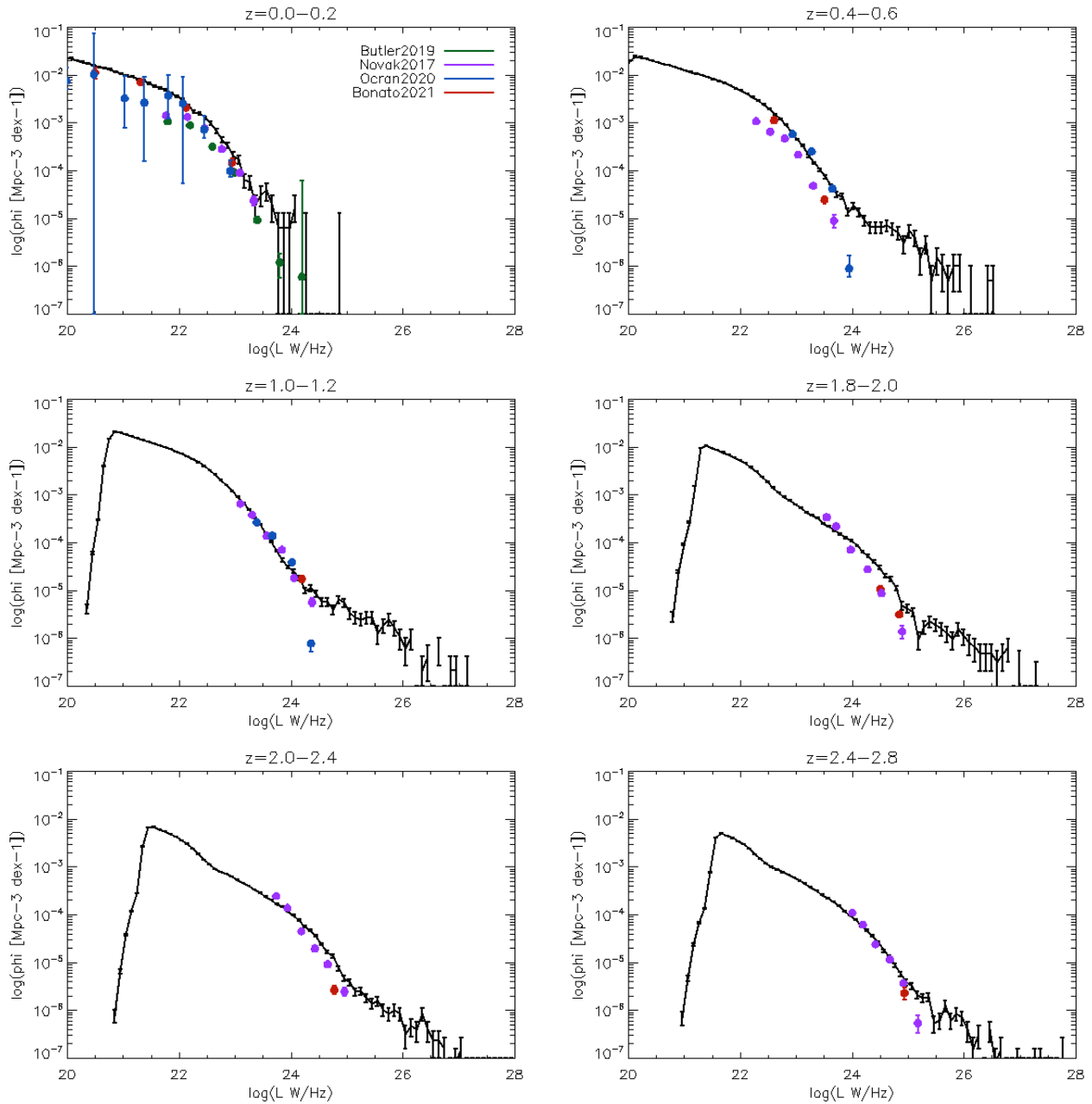


Figure 3. Comparison of continuum luminosity functions between T-RECS and the available data from Novak et al. (2017); Butler et al. (2019); Ocran et al. (2020); Bonato et al. (2021)

mass distribution matches well the mass function from the P-millennium (Baugh et al. 2019) cosmological simulation, which is used to simulate clustering (see Sec. 5 for more details).

The DM mass modelling is the same as T-RECS I. For SFGs, we used a $L_{\text{SFR}}-M_{\text{h}}$ relation of the form:

$$L(M_{\text{h}}) = N \times \left[\left(\frac{M_{\text{h}}}{M_b} \right)^\alpha + \left(\frac{M_{\text{h}}}{M_b} \right)^\omega \right]^{-1}, \quad (10)$$

where N , α , ω and M_b are free parameters which include redshift evolution. We start from the Baugh et al. (2019) target halo mass function as a function of redshift, and we derive the parameters so that the resulting luminosity function

matches as closely as possible the radio luminosity function at 1.4 GHz from Bonato et al. (2017). Once the parameters are derived, eq. (10) can be inverted to obtain M_{h} from the 1.4 GHz luminosity.

For RL AGN, we start again from the halo mass function of the Baugh et al. (2019) simulation to draw a sample of galaxies with plausible DM mass distribution for each T-RECS redshift interval. For all galaxies in the sample, we compute the stellar mass with the Aversa et al. (2015) $M_{\text{star}} = F(M_{\text{h}})$ relation (their Table 2, including redshift evolution).

Janssen et al. (2012) derived the fraction of galaxies

hosting an RL AGN as a function of the host galaxy stellar mass, M_{star} , separately for Low Excitation Radio Galaxies (LERGs) and High Excitation Radio Galaxies (HERGs). We use this result to extract subsamples of HERGs and LERGs from the initial galaxy sample. We finally compute the M_{h} distribution of the two sub-samples, which, once appropriately normalised, can be used to draw halo masses suitable for a HERG/LERG host. We map the HERG/LERG populations into our T-RECS observational categories as follows: FSRQs to the HERG population; BL Lacs to the LERG population; SS-AGN morphologically classified as FR II/FR I to the HERG/LERG population (see TRECS I for more details).

3.4 HI mass modelling from radio continuum properties

The interplay between gas and stars in the lifecycle of a galaxy results in a correlation between HI mass, stellar mass, and SFR, which is exemplified by the Kennicutt-Schmidt Law (Kennicutt 1998). Scaling relations between HI mass tracers and SFR tracers have been derived (e.g. Zhou et al. 2018; Bothwell et al. 2013; Catinella et al. 2010; Cortese et al. 2011; Jaskot et al. 2015; Huang et al. 2012; Sinigaglia et al. 2022, just to cite some of the most recent); the correlation is well established, with a scatter indicative of the many factors that regulate SFR. Among those, there is feedback from AGN activity, that heats the surrounding gas therefore reducing star formation. Additionally, an important role is played by galaxy type. Late-type galaxies, associated with spiral/disk morphologies, are typically HI-rich and actively forming stars, while early-type galaxies, with spheroidal/elliptical morphology, are typically HI-poor and have low star formation.

The SFR- M_{HI} correlation mentioned above provides a relatively straightforward way to add HI mass to the modelling of T-RECS star-forming galaxies. We call this HI mass \tilde{M}_{HI} , to distinguish it from the HI mass modelled for HI sources in Sec. 2. It can be written as:

$$\log(\tilde{M}_{\text{HI}}) = A \log(\text{SFR}) + B \quad (11)$$

with a scatter σ ; the slope and normalization A and B are in general redshift-dependent.

We derive the parameters A and B by imposing that the resulting \tilde{M}_{HI} distribution is consistent with the HI mass function adopted for the HI model in Sec. 2. The redshift evolution as in Paul et al. (2023) means that the maximum HI mass changes relatively rapidly as a function of redshift. The evolution of the SFR function in Mancuso et al. (2015) is not as fast, and imparts a significant redshift dependence of the parameters A and B . We find that

$$A(z) = 1.1 - 2.46z + 2.06z^2 \quad (12)$$

$$B(z) = 9.5 - z \quad (13)$$

and a scatter $\sigma \log \tilde{M}_{\text{HI}} = 0.2$ give a good agreement in the considered redshift range.

In Fig.5 we show the $\log(\text{SFR})$ - $\log(\tilde{M}_{\text{HI}})$ relation for the T-RECS catalogue up to $z = 0.3$ compared to the best fits from Naluminsa et al. (2021), Cluver et al. (2014) and Michałowski et al. (2015). The slope of the correlation is consistent with the observational estimates. However, our

normalization is higher, at $\Delta \log(\text{SFR}) \sim 0.3$ - 0.4 . Using one of the observed relations instead of the abundance-matching parameters produces larger HI masses than what would be consistent with the HI mass function by Jones et al. (2018) plus redshift evolution. In other words, this is essentially a tension between the Mancuso et al. (2015) model of SF and the Jones et al. (2018) HI mass function, which indicates that there is still some distance to cover to get a consistent model across both observables.

Several relations have been published between M_{HI} and the stellar mass, M_{star} (e.g. Catinella et al. 2010; Huang et al. 2012; Maddox et al. 2015; Naluminsa et al. 2021), which could be used as an HI mass proxy for the AGN population. The relation appears to be linear at the low-mass end, and to flatten at the high-mass end due to the dominance of early-type, HI-poor galaxies. We adopt the maximum likelihood relation by Naluminsa et al. (2021) up to $M_{\text{star}} = 10^{10} M_{\odot}$ and Catinella et al. (2010) for higher masses. The latter was derived on an unbiased sample of galaxies selected by stellar mass and therefore should contain the gas-poor systems that are typically missed by the current untargeted HI surveys.

In Fig. 1 we compare the HI mass function (black line and symbols) with the HI continuum mass proxy distribution (red symbols). Overall, there is a satisfactory agreement between the two, ensured by the abundance-matching method used to derive the parameters in eq. (11), as well as a plausible modelling of the HI mass proxy for the AGN population.

The discrepancy at the low-mass end is due to the different selection functions. As mentioned, the selection in HI flux almost corresponds to a selection in mass, and gives high completeness of the sample down to the last mass bin. Conversely, the selection in continuum flux means that the mass proxy sample is progressively incomplete. Departures from the two distributions not due to completeness can be ascribed to the simplicity of eq. (11), which cannot guarantee a perfect fit over the whole mass range. At the high-mass end, the mass-proxy distribution tends to over-predict the number of objects. This region of the distribution contains very few objects, and therefore its weight in the abundance-matching scheme is relatively low.

4 CONTINUUM \times HI MODEL

So far, the T-RECS HI and continuum produced with the modules described in Secs. 2 and 3 are independent. Each produces statistically plausible samples of sources, but the two samples are uncorrelated and have different sky coordinates.

If the two catalogues were used to represent the same area of the sky, one would expect a certain number of positional cross-matches between the two, as the same galaxy is visible in both bands. In this section, we discuss how a consistent HI \times continuum catalogue can be constructed by associating counterparts between the two catalogues and rewriting one of the two coordinate sets to match.

First of all, counterparts are only explored between galaxies that belong to the same redshift slice between the two simulations. We consider a sample $\{i\}$ of continuum sources and $\{j\}$ of HI sources, which have been selected

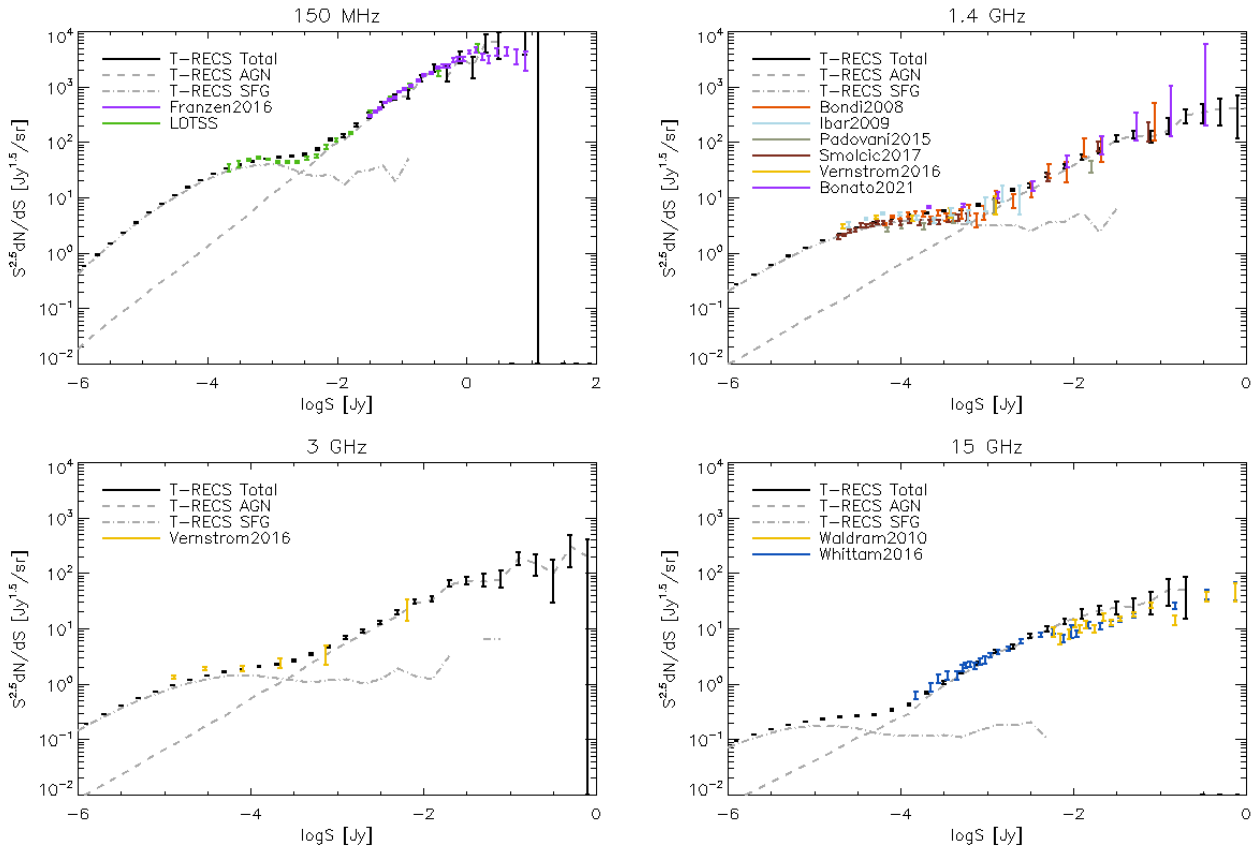


Figure 4. Comparison of differential source counts in total intensity at 150 MHz (top left) 1.4 GHz (top right), 3 GHz (bottom left) and 15 GHz (bottom right) between T-RECS and the available data from Franzen et al. (2016); Bondi et al. (2008); Vernstrom et al. (2016); Smolčić et al. (2017); Padovani et al. (2015); Ibar et al. (2009); Whittam et al. (2016); Waldram et al. (2010); AMI Consortium et al. (2011); Mandal et al. (2021); Bonato et al. (2021)

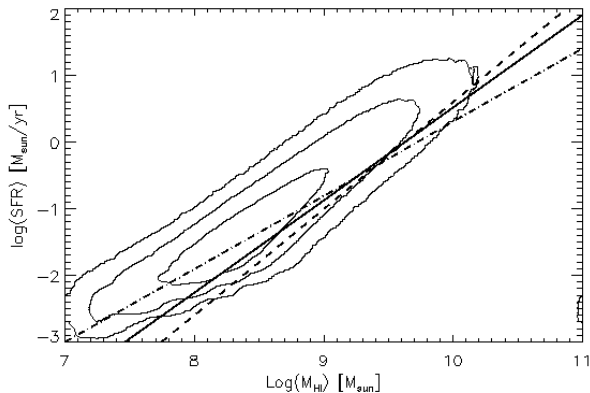


Figure 5. Relation between SFR and \tilde{M}_{HI} for the $z \leq 0.3$ continuum catalogue, compared to Naluninsa et al. (2021) (dashed line), Cluver et al. (2014) (dot-dashed line) and Michałowski et al. (2015) (solid line). Contours include are 99%, 90% and 50% of all galaxies.

with $S^i > S1$ and $f_{\text{HI}}^j > F1$, where S^i are the fluxes in continuum, f_{HI}^j the fluxes in HI, and $S1$, $F1$ are the respective detection limits. If we ignore redshift variation within a slice, from eq. (1) we can rewrite the HI selection in terms

of HI mass, as $M_{\text{HI}}^j > M1$ where M_{HI}^j and $M1$ are the HI masses corresponding to f_{HI}^j and $F1$ at the given redshift.

The counts of both the $\{i\}$ and $\{j\}$ samples come from the appropriately normalised distributions (luminosity function, SFR function and HI mass function) and need to be conserved. Therefore, all objects are retained, and in general only some of them have a counterpart. Based on the HI selection function, continuum sources belonging to $\{i\}$ would be visible also in HI if their HI mass is above $M1$. Assessing this requires a modelling of the HI mass for the continuum sources, \tilde{M}_{HI}^i , which we have introduced and described in Sec. 3.4.

We note that \tilde{M}_{HI}^i does not come from sampling an expected HI mass distribution and so selecting a subsample of potential counterparts as $\tilde{M}_{\text{HI}}^i > M1$ would not automatically reproduce HI source counts and could lead to objects that are mismatched with $\{j\}$. However, if we have compatible \tilde{M}_{HI} and M_{HI} distributions, the differential counts are similar $N(M_{\text{HI}}) \sim N(\tilde{M}_{\text{HI}})$ and so are the number of sources above the same mass limit. In this case, assigning counterparts based on matching M_{HI} from the HI catalogue with \tilde{M}_{HI} from the continuum catalogue produces a similar selection function.

As already discussed in Sec. 3.4, our modelling of \tilde{M}_{HI} for the SFGs, which are the vast majority of the continuum

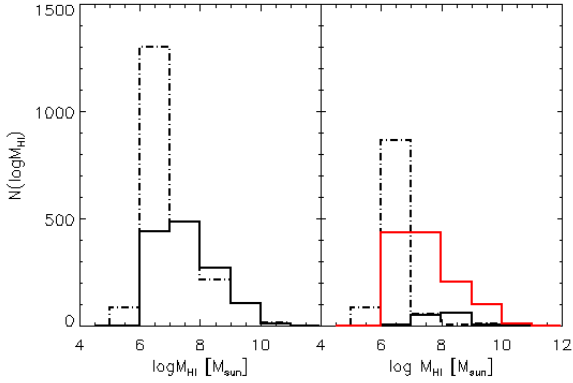


Figure 6. *Left:* Distribution of M_{HI} for an HI catalogue of 25 deg^2 $f_{\text{HI}} \geq 1 \text{ Jy/Hz}$ and $z = 0.475\text{--}0.525$ (solid line) and of \tilde{M}_{HI} for a continuum catalogue with the same sky area and redshift range and $S_{1.4 \text{ GHz}} \geq 100 \text{ nJy}$ (dot-dashed line). *Right:* distribution of M_{HI} for the cross-matched catalogue (red solid line); HI unmatched sources (black solid line) and continuum unmatched sources (black dot-dashed line).

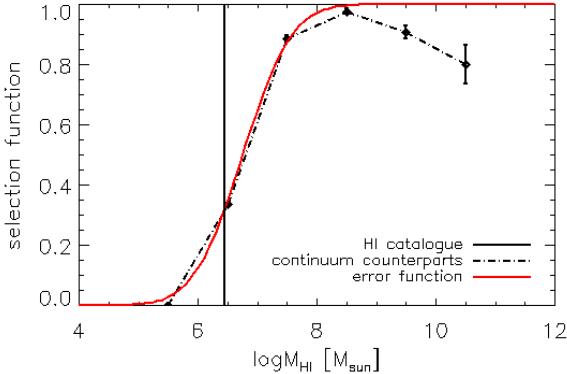


Figure 7. Selection function as a function of HI mass for the HI catalogue (black solid line) and the matched continuum counterparts (black diamonds and dot-dashed line) for the example in Fig. 6. Superimposed in red is the theoretical selection function corresponding to a Gaussian error $\sigma \log M = 0.65$ and an offset $\Delta \log M = 0.3$, which is a good fit to the observed selection.

sources, has been explicitly designed to reproduce the HI mass function as best as possible, by using an abundance-matching technique to constrain its parameters (see also Fig 1). The mass match ensures that broadly compatible objects between the two catalogues are assigned, and it propagates, although with additional scatter, the modelled correlations between continuum and HI properties. For example, the SFR– M_{HI} correlation that has been modelled for the continuum catalogue shown in Fig. 5 is conserved when we consider the HI \times continuum catalogue.

The HI selection $M_{\text{HI}}^j > M1$ maps to a selection in \tilde{M}_{HI}^j which is smoother than the original step function, due to the various uncertainties introduced by the additional modelling.

The HI mass-matching itself is performed with a nearest neighbour implementation. Initially, for each galaxy in

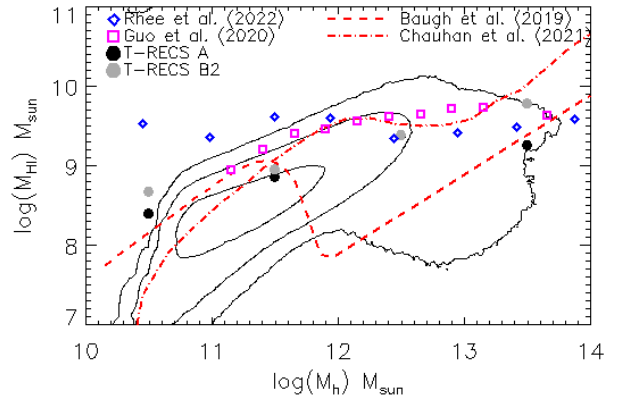


Figure 8. Median T-RECS $M_{\text{h,cont}}\text{--}M_{\text{HI}}$ (T-RECS 1) and $M_{\text{h,HI}}\text{--}M_{\text{HI}}$ (T-RECS 2) compared to HI–halo mass relation from observations (Guo et al. 2020; Rhee et al. 2023, central galaxies only) and theoretical modelling (Baugh et al. 2019; Chauhan et al. 2021). The contours are the full distribution for the T-RECS 1 model, including 99%, 90% and 10% of the galaxies.

the HI catalogue, the 20 nearest neighbours from the continuum catalogue are retained, as counterpart candidates. The HI galaxies are then reprocessed in order of decreasing HI mass, and a unique counterpart is assigned to each of them, if available, as the best of the 20 candidates that has not been already matched. The 20 nearest neighbours have been chosen as a trade-off between computational speed and having enough samples for a good mass-matching. The reason for proceeding in inverse mass order is that high-mass objects are more rare and therefore more difficult to match accurately, but at the same time brighter and therefore more likely to have a counterpart.

In the left panel of Fig. 6 we show the histograms of the HI masses M_{HI} for an HI catalogue with $f_{\text{HI}} > 1 \text{ Jy/Hz}$ and \tilde{M}_{HI} for a continuum catalogue with $S_{1.4 \text{ GHz}} > 100 \text{ nJy}$, over 25 deg^2 and $z = 0.5$. The HI catalogue has a mass limit $\log M1 = 6.45$. Similar numbers of galaxies are available in both catalogues as a function of M_{HI} for $\log M_{\text{HI}} \geq 7$. In the $\log M_{\text{HI}} = 6$ mass bin, the counts $N(M_{\text{HI}})$ and $N(\tilde{M}_{\text{HI}})$ start to diverge, and there is an excess of sources in the continuum catalogue.

In the right panel of Fig. 6 we show the mass distribution of the cross-matched catalogue with the red line, and the unmatched sources with the black solid line and the black dash-dotted line for HI and continuum, respectively. In this case, the continuum is deeper than the HI and most HI sources have a continuum counterpart. When considering another couple of catalogues with different detection limits, the proportion of sources in the matched, HI-only and continuum-only categories would change. The $M_{\text{HI}}\text{--}\tilde{M}_{\text{HI}}$ relation for the matched objects is very tight, with $\log M_{\text{HI}} - \log \tilde{M}_{\text{HI}} = 2.4 \pm 9.4 \times 10^{-3}$.

In Fig. 7 we compare the selection in mass of the HI catalogue ($\log M1 > 6.45$) with that of the matched continuum counterparts (diamonds and dot-dashed line). The error bars are consistent with Poisson statistics and reflect the very different number of sources that are present in the different mass bins.

In the Gaussian approximation, for a scatter σ_M on the mass M and a detection limit M_1 , the selection function $F(M)$ is an error function

$$F(M) = \frac{1}{2} \left[1 - \operatorname{erf} \left(\frac{M_1 - M}{\sigma_M \sqrt{2}} \right) \right]. \quad (14)$$

The red line in Fig. 7 is an error function similar to the measured selection, which corresponds to a mass limit $\log \tilde{M}_1 = 6.75 \pm 0.65$. The scatter is due to that of the SFR– \tilde{M}_{HI} relation and that of the mass matching. The offset $\Delta \log M = 0.3$ is due to differences in the distributions of \tilde{M}_{HI} and M_{HI} , in particular the excess of continuum sources in the $\log M_{\text{HI}} = 6$ mass bin. At the highest masses, the observed selection departs from the error function, with a few radio continuum galaxies not having an HI counterpart. This is due to discrepancies between the high-mass end of the HIMF and the HI mass proxy distribution (see also Fig 1).

The difficulty in accurately reproducing the expected HI mass function starting from a radio continuum catalogue is one of the reasons behind our choice to model the HI independently and then cross-match with the continuum catalogue. In this way those discrepancies, rather than affecting the number of HI sources for an HI selection, only affect the number of continuum counterparts.

We note that the method we described does not necessarily identify pairs of galaxies that are the most consistent in terms of properties other than the HI mass. To achieve this, a better approach would be to simultaneously match multiple catalogue attributes at once, for example M_h , M_{star} and M_{HI} . However, this approach would increase the scatter between the matched \tilde{M}_{HI} and M_{HI} which would result in a selection of the continuum sources largely independent from the HI signal strength.

We point out that the selection functions adopted in T-RECS are an approximation of what actually achieved by real observations. In radio continuum, the ability to detect a source of a given integrated flux density depends, amongst other things, on how much of that flux is contained within the instrumental point spread function. Similarly, completeness for a given HI flux depends on the 3D size and shape of the source, particularly the line width, with sources having narrower line widths being easier to detect (see, e.g., Haynes et al. 2011). Instrumental specifications, such as spatial and spectral resolution, need to feature in an accurate description of selection functions. Additionally, an important role is played by the adopted source finding algorithms, which perform spatial and spectral filtering of the sources to maximise detection (see, e.g. Bonaldi et al. 2021; Hartley et al. 2023, for a comparison of different source finding methods on the same data). If the goal is to accurately reproduce the selection functions of specific surveys, T-RECS catalogues should be generated with flux limits consistent with the deepest achievable fluxes, and further filtering of the source lists should be performed on additional source properties, as appropriate.

5 CLUSTERING

As described in T-RECS I, the clustering properties of the sources are simulated by associating each galaxy with a

dark matter sub-halo of the P-millennium (Baugh et al. 2019) cosmological simulation. The cosmological parameters adopted in this simulation are: $H_0 = 67.77 \text{ km s}^{-1} \text{ Mpc}^{-1}$, $\Omega_\Lambda = 0.693$, $\Omega_M = 0.307$, $\sigma_8 = 0.8288$ (Planck Collaboration XVI 2014).

The reason for choosing this simulation is its very high mass resolution, which means that sub-haloes are tracked individually down to $M_h = 1.6 \times 10^9 M_\odot$, but also a large box size (800 comoving Mpc/h). The latter allows producing a $5 \times 5 \text{ deg}^2$ lightcone up to $z = 8$, which is therefore the maximum T-RECS survey size for which we can simulate clustering. This approach essentially matches galaxies to haloes by means of the dark mass M_h , separately for each redshift slice, and overwrites the T-RECS latitude, longitude and redshift coordinates with those of the matched haloes. The clustering is therefore simulated in 3 dimensions.

Two predictions for the dark matter mass of T-RECS galaxies are available: $M_{h,\text{HI}}$ as modelled from the HI properties in Sec 2, and $M_{h,\text{cont}}$ as modelled from the radio continuum properties for SFGs and AGN in Sec 3. Given the uncertainties related with both modelling and measurement of dark matter mass, both quantities are retained as alternative models in an HI \times continuum catalogue.

Several works have explored the total HI mass in dark matter haloes (HI-halo mass relation, HIHM), which is important to understand the role of HI in galaxy formation and its connection to structure formation. This relation has been investigated extensively in different theoretical models (Barnes & Haehnelt 2014; Paul et al. 2018; Obuljen et al. 2019; Kim et al. 2017; Villaescusa-Navarro et al. 2018) and observationally, via spectral stacking (Guo et al. 2020; Rhee et al. 2023). Theoretical studies predict a positive correlation between M_h and M_{HI} in both the low- M_h regime, which is dominated by central galaxies, and the high- M_h regime, dominated by groups and satellite galaxies. The overall relation has a flattening at masses in between these two regimes. Observational estimates have so far measured a much flatter relation, with M_{HI} only mildly depending on M_h . Possible observational biases to account for these discrepancies are discussed in details in Chauhan et al. (2021).

In Fig. 8 we compare the $M_{h,\text{HI}}-M_{\text{HI}}$ (T-RECS B) and $M_{h,\text{cont}}-M_{\text{HI}}$ (T-RECS A) relations with some of the HIHM in the literature. They can only be qualitatively compared, since T-RECS's are galaxy-galaxy relations and the HIHM is the total HI content of haloes including multiple galaxies. The comparison is more meaningful at the lowest halo masses, where a single galaxy occupancy of haloes is prevalent, or when considering the central galaxies' contribution to the total HIHM. The filled circles show the median T-RECS A and T-RECS B relations; black contours are the full T-RECS A $M_{h,\text{cont}}$ model including 99%, 90% and 50% of the galaxies. Diamonds and squares are the central galaxies' observational relations by Rhee et al. (2023) and Guo et al. (2020). Dashed and dash-dotted lines are the theoretical relations by Baugh et al. (2019) and Chauhan et al. (2021). Error bars on the observational estimates have been omitted for figure clarity.

The T-RECS A model is in qualitatively good agreement with both the observational estimates and with the Chauhan et al. (2021) model over the mass range $10^{11} < M_h < 10^{13} M_\odot$. It also manages to reproduce the flattening of the relation towards high masses, which in T-RECS is the

Table 1. Comparison on the selection between different radio continuum clustering estimates in the literature

Observation	ν [GHz]	$S_{\text{limit},\nu}$ [mJy]	Ref.
COSMOS	3	0.013	Hale et al. (2018)
COSMOS	1.4	0.15	Magliocchetti et al. (2017)
LH	1.4	0.15	Bonato et al. (2021)
EN1	0.612	0.05	Chakraborty et al. (2020)

result of associating some HI galaxies to AGN sources, which typically have a larger halo mass. The T-RECS B model does not present any flattening and it predicts a higher HI mass for the same dark mass. This is because the relation used to model $M_{\text{h,HI}}$ has been derived for late-type galaxies, which have higher HI fraction. As such, this relation fails to capture the most massive, early-type galaxies which are HI-poor. A lower DM mass for these sources would result in lower clustering. For this reason, in the clustering analysis that follows, the dark matter mass of the continuum counterpart $M_{\text{h,cont}}$ has been used, whenever present.

The implementation of the DM mass matching is based on the same nearest-neighbour approach used for the M_{HI} mass matching in Sec. 4. Given the very large number of DM sub-haloes contained in the lightcone, however, comparing every galaxy to every halo is a significant bottleneck in terms of execution time. At low M_{h} especially, there is an overabundance of DM haloes with respect to galaxies, due to the shape of the DM mass function and selection effects for the T-RECS catalogues. On those mass ranges, and depending on the sizes of the samples to be compared, a subsample of the available sub-haloes can be randomly selected for the subsequent analysis. This has very significant advantages in terms of computational cost, at the price of a negligible increase of the scatter between the matched masses.

5.1 Validation for continuum sources

Several observational estimates of clustering for AGN and SFGs are present in the literature (Magliocchetti et al. 2017; Hale et al. 2018; Chakraborty et al. 2020; Bonato et al. 2017). Details of the source selection for those studies are collected in Table 1.

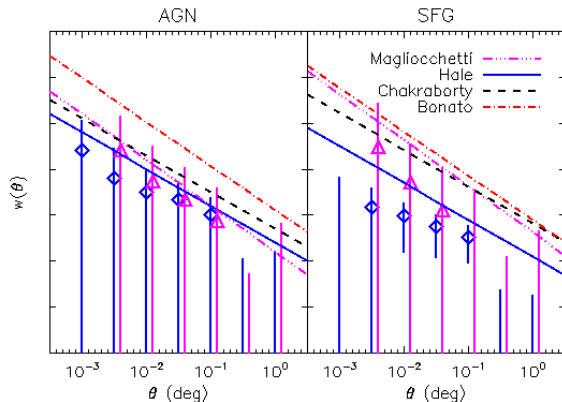
The observational estimates adopted the standard power-law shape for the two-point angular correlation function: $w(\theta) = A\theta^{1-\gamma}$. Since the data did not allow an accurate determination of both A and γ for each source population, they fixed γ and fit for the normalization.

To produce the T-RECS correlation functions we use the same flux limits of the observational estimates and a sky area of 4×4 square degrees. We use the Hamilton (1993) estimator:

$$w(\theta) = \frac{DD \cdot RR}{DR \cdot DR} - 1, \quad (15)$$

where DD , RR and DR are the number of data-data, random-random and data-random pairs separated by θ .

The random catalogue is constructed by allocating a random position of all sources within the simulated sky area. The $w(\theta)$ is computed for 500 realizations. Each realization uses a different generation of the continuum catalogue and a different $4 \times 4 \text{ deg}^2$ portion of the DM lightcone, which is extracted from the $5 \times 5 \text{ deg}^2$ with a random uniform shift from the field centre in both coordinates.

**Figure 9.** Two-point angular correlation function $w(\theta)$ yielded by our simulation (symbols with error bars) for radio AGN (left) and SFGs (right) compared to the observational results in Table 1 (coloured lines).

In Fig. 9 we show the mean observational estimates as lines of different colours. Uncertainties have not been included, in order to improve figure clarity. The different selection criteria are responsible for some of the differences in the measured clustering. At the same selection frequency, a deeper flux limit would correspond to less luminous sources, which are expected to be found in less massive, weakly clustered haloes. Therefore, deeper catalogues find a lower normalization of the correlation function. A different selection frequency would favour different sub-populations, which could have different clustering properties.

T-RECS mean values and their dispersion for catalogues with flux limits as in Magliocchetti et al. (2017) and Hale et al. (2018) are shown as symbols and error bars with the same colour as the observational estimates. For the same source selection, our simulations give amplitudes of the angular correlation function consistently lower than the observational ones.

The higher amplitudes of the observationally estimated $w(\theta)$ imply higher average bias factors, i.e. higher halo masses. As already discussed in T-RECS I, various factors can influence the comparison between the observational determinations and the T-RECS simulations. One of those is the observational classification between AGN and SFG and how this compares with the definition of the two populations in T-RECS. Another factor is the availability of high-mass haloes in the Baugh et al. (2019) cosmological simulation adopted in T-RECS. The mass function of the cosmological simulation and that inferred from the luminosity function are somewhat different, which means that there is a deficit of suitable haloes in some mass ranges and a surplus in others. Allowing for some scatter between the predicted and the associated mass alleviates the problem; however, it typically favours association to smaller halo masses, given the shape of the mass function.

T-RECS results are still consistent with the observations using the same flux limit, with the exception of Hale et al. (2018) SFGs. In the latter case the discrepancy is of 2.5σ , where σ is the quadratic sum of errors of the observational estimates and of the simulations.

Despite the differences noted above, and taking into ac-

count the uncertainties in both determinations, the agreement between the T-RECS clustering and the empirically-determined one is reasonably good.

5.2 Validation for HI sources

Observational estimates of the real-space correlation functions for galaxies selected in HI are presented by Passmoor et al. (2011), Martin et al. (2012) and Papastergis et al. (2013). Details of the survey used are reported in Table 2. The observational estimates adopt a power-law model for the correlation function of the form $\xi(r) = (r/r_0)^{-\gamma}$, and fit for both the r_0 and the γ parameters.

We select T-RECS sources with a mass limit of $\log M_{\text{HI}} = 7.5 M_{\odot}$ and a redshift limit of $z = 0.05$, in an attempt to be comparable with the observational estimates. However, the observed samples have a complex selection function and they are neither flux- or mass-limited, which makes the comparison of the results more complicated.

In order to get good statistics for the computation of $\xi(r)$, we use the maximum possible area for a T-RECS clustered simulation, of 25 deg^2 . Observational estimates were obtained within larger surveys, of $\sim 400 \text{ deg}^2$ for ALFALFA and $29,000 \text{ deg}^2$ for HIPASS.

To produce T-RECS correlation functions we use again the estimator in eq. (15); we checked that using the Landy & Szalay (1993) estimator as in Passmoor et al. (2011), Martin et al. (2012) and Papastergis et al. (2013) gives comparable results. For the random catalogue we use the unclustered T-RECS catalogue, which therefore has a plausible redshift distribution and random angular coordinates within the simulated sky area. The clustered catalogue contains the same sources, but the angular and redshift coordinates are replaced with those of dark haloes in the same redshift range that have similar mass.

The $\xi(r)$ is computed for 500 realizations. Each realization uses a different generation of both the HI and continuum catalogue (which is also used in the dark mass matching process, as previously explained).

In Fig. 10 we show the comparison between T-RECS and the observational estimates (uncertainties in the latter were not included to improve figure clarity). T-RECS results reproduce the slope of the observations and are lower in amplitude; the discrepancy is of $1.5\text{--}2.5\sigma$ depending on the dataset.

As previously mentioned, this comparison is made more difficult by the different source selection. T-RECS sources are complete down to $M_{\text{HI}} = 10^{7.5}$. This is the minimum mass achieved by the observational samples (specifically, Papastergis et al. 2013), which could in part explain the lower normalization. The HI catalogue would also most likely inherit the same issue of the continuum catalogue, that has to do with the availability of high-mass haloes in the cosmological simulation.

6 CONCLUSIONS

This work updated the T-RECS radio continuum model presented in Bonaldi et al. (2019) to improve the agreement with the most recent observations and extended it to in-

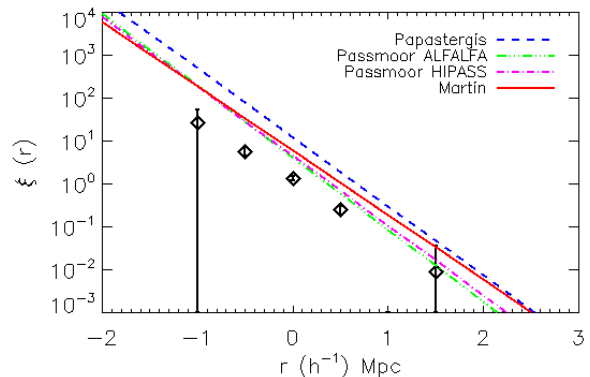


Figure 10. Real-space correlation function $\xi(r)$ yielded by our simulation (symbols with error bars) compared to the observational results in Table 2 (coloured lines).

clude HI emission from extra-galactic sources as well as the cross-correlation between the two.

The HI model reproduces the Jones et al. (2018) HI mass function and the Oman (2022) HI velocity width function at $z = 0$. Evolution of the HI mass function has been modelled as a linear dependence of the $\log(M_{\text{HI}}^*)$ and $\log \phi^*$ parameters with redshift, with amplitudes calibrated to give results consistent with Paul et al. (2023) at $z = 0.3$. Uncertainties in this modelling are due to a lack of high-redshift data and currently limit our HI simulation to a maximum redshift of 0.5. The HI model further includes source size (modelled with the $\log M_{\text{HI}} - \log D_{\text{HI}}$ relation by Naluminsa et al. 2021) and morphology (galaxy type, inclination, ellipticity using Holmberg 1958 and Rodriguez & Padilla 2013).

The updated radio continuum model makes use of a steepening synchrotron spectral index and the Smith et al. (2021) $L(\text{SFR}) - M_{\text{star}}$ relation. The goodness of the model has been evaluated by comparing T-RECS realizations with observed luminosity functions at 1.4 GHz as well as the most recent compilations of number counts in the 150 MHz–15 GHz. We also modelled an HI mass proxy for the continuum sources, \tilde{M}_{HI} , by using the SFR– M_{HI} correlation for star-forming galaxies and published relations between the HI mass and the stellar mass for the AGN.

We showed that, by matching the HI mass proxy in the continuum catalogue with the HI mass in the HI catalogue, we are able to assign plausible counterparts between the otherwise independent T-RECS continuum and HI simulations. Our method ensures a correct number of counterparts by applying an HI selection function to the radio continuum sources consistent with that of the HI catalogue, within an error $\sigma_{\log M} \sim 0.65$. It also propagates modelled correlations between the radio continuum and HI properties via their link to M_{HI} .

The $M_{\text{h}} - M_{\text{HI}}$ relation for T-RECS galaxies is qualitatively in good agreement with the HI–halo mass relation from data (Guo et al. 2020; Rhee et al. 2023) and theoretical modelling (Chauhan et al. 2021).

Clustering properties were simulated by associating the galaxies with haloes of the P-millennium (Baugh et al. 2019) simulation of similar dark halo mass. We assessed the clustering properties of both the HI and the continuum cata-

Table 2. Details of the samples used for HI clustering estimates in the literature. Values of mass denoted with * are average masses rather than lowest masses.

Observation	v_{\max} [km/s]	z_{\max}	$M_{\text{HI},\min}$ [M_{\odot}]	Ref.
ALFALFA	15,000	0.05	$10^{7.5}$	Papastergis et al. (2013)
ALFALFA	15,000	0.06		Martin et al. (2012)
HIPASS	12,700	0.06	$3.24 \cdot 10^9$ *	Passmoor et al. (2011)
ALFALFA	18,000	0.06	$2.48 \cdot 10^9$ *	Passmoor et al. (2011)

logue and validated them against the empirical estimates of $w(\theta)$ (Magliocchetti et al. 2017; Bonato et al. 2021; Chakraborty et al. 2020) and $\xi(r)$ (Passmoor et al. 2011; Martin et al. 2012; Papastergis et al. 2013). The T-RECS simulation correctly reproduces the slope of both correlation functions. The normalization is in both cases lower (of $1.5\text{--}2.5\sigma$). This could be explained at least in part by the difficulty in reproducing the selection functions of the observational estimates; issues with the availability of high-mass haloes in the Baugh et al. (2019) dark matter simulation we derived the clustering from could also be responsible.

The code used to produce these results is available on github (<https://github.com/abonaldi/TRECS.git>) and can be used to produce mock observations of radio continuum and HI observations, as well as their cross-correlation. We believe these can be very useful to plan for future surveys. This code has been used as a basis of the second science data challenge (SDC2 Hartley et al. 2023) organised by the SKA Observatory to prepare the science community to analyse SKA HI data.

ACKNOWLEDGEMENTS

We thank M. Massardi, V. Galluzzi, A. Lapi, I. Prandoni for useful suggestions on how to update the T-RECS continuum model. We thank S. Blyth for her useful comments on the paper. We also thank the anonymous referee for their review, that has led to a substantial improvement of this work.

We acknowledge the use of computational resources at the SKA Observatory.

TR is supported by the PRIN MIUR 2017 prot. 20173ML3WW, ‘Opening the ALMA window on the cosmic evolution of gas, stars and supermassive black holes’, and by the Fondazione ICSC - Spoke 3 Astrophysics and Cosmos Observations - National Recovery and Resilience Plan Project ID CN-00000013 ‘Italian Research Center on High-Performance Computing, Big Data and Quantum Computing’ - Next Generation EU.

We acknowledge usage of the Fortran (Backus & Heising 1964) and Python (Van Rossum et al. 2007) programming languages, Astropy (The Astropy Collaboration et al. 2013), NumPy (Harris et al. 2020), Scikit-learn (Pedregosa et al. 2011), LAPACK (Anderson et al. 1999), GSL (Galassi et al. 1996), HEALPix (Gorski et al. 2005), CFitsIO (Pence 2010).

DATA AVAILABILITY

The data underlying this article are available at the link <https://tinyurl.com/TRECS2>. The code used to generate the data is available on Github (<https://github.com/abonaldi/TRECS.git>)

References

- Adams, E. A. K., Adebahr, B., de Blok, W. J. G., et al., 2022, *A&A*, 667, A38, arXiv:2208.05348
- AMI Consortium, Davies, M. L., Franzen, T. M. O., et al., 2011, *MNRAS*, 415, 2708, arXiv:1012.3659
- Anderson, E., Bai, Z., Bischof, C., et al., 1999, *LAPACK users’ guide*, SIAM
- Aversa, R., Lapi, A., de Zotti, G., Shankar, F., Danese, L., 2015, *ApJ*, 810, 74, arXiv:1507.07318
- Backus, J. W., Heising, W. P., 1964, *IEEE Transactions on Electronic Computers*, , 4, 382
- Barnes, D. G., Staveley-Smith, L., de Blok, W. J. G., et al., 2001, *MNRAS*, 322, 3, 486
- Barnes, L. A., Haehnelt, M. G., 2014, *MNRAS*, 440, 3, 2313, arXiv:1403.1873
- Baugh, C. M., Gonzalez-Perez, V., Lagos, C. d. P., et al., 2019, *MNRAS*, 483, 4, 4922, arXiv:1808.08276
- Bera, A., Kanekar, N., Chengalur, J. N., Bagla, J. S., 2022, *ApJ*, 940, 1, L10, arXiv:2210.17018
- Blyth, S., Baker, A. J., Holwerda, B., et al., 2016, in *MeerKAT Science: On the Pathway to the SKA*, 4
- Bonaldi, A., An, T., Brügger, M., et al., 2021, *MNRAS*, 500, 3, 3821, arXiv:2009.13346
- Bonaldi, A., Bonato, M., Galluzzi, V., et al., 2019, *MNRAS*, 482, 1, 2, arXiv:1805.05222
- Bonato, M., Negrello, M., Mancuso, C., et al., 2017, *MNRAS*, 469, 2, 1912, arXiv:1704.05459
- Bonato, M., Prandoni, I., De Zotti, G., Brienza, M., Morganti, R., Vaccari, M., 2021, *MNRAS*, 500, 1, 22, arXiv:2010.08748
- Bondi, M., Ciliegi, P., Schinnerer, E., et al., 2008, *ApJ*, 681, 1129, arXiv:0804.1706
- Bothwell, M. S., Maiolino, R., Kennicutt, R., et al., 2013, *MNRAS*, 433, 2, 1425, arXiv:1304.4940
- Broeils, A. H., Rhee, M. H., 1997, *A&A*, 324, 877
- Butler, A., Huynh, M., Kapińska, A., et al., 2019, *A&A*, 625, A111, arXiv:1904.12507
- Catinella, B., Schiminovich, D., Kauffmann, G., et al., 2010, *MNRAS*, 403, 2, 683, arXiv:0912.1610
- Chakraborty, A., Dutta, P., Datta, A., Roy, N., 2020, *MNRAS*, 494, 3, 3392, arXiv:2002.12383

² The full link is <https://www.dropbox.com/sh/52pbxscr8pkrdn7/AAA-RPe6QcTeQrcqEvNpSWkoa?dl=0>

- Chauhan, G., Lagos, C. d. P., Stevens, A. R. H., et al., 2021, *MNRAS*, 506, 4, 4893, arXiv:2102.12203
- Cluver, M. E., Jarrett, T. H., Hopkins, A. M., et al., 2014, *ApJ*, 782, 2, 90, arXiv:1401.0837
- Cortese, L., Catinella, B., Boissier, S., Boselli, A., Heinis, S., 2011, *MNRAS*, 415, 2, 1797, arXiv:1103.5889
- De Zotti, G., Ricci, R., Mesa, D., et al., 2005, *A&A*, 431, 893, astro-ph/0410709
- DiPompeo, M. A., Runnoe, J. C., Myers, A. D., Boroson, T. A., 2013, *ApJ*, 774, 24, arXiv:1307.1731
- Duffy, A. R., Meyer, M. J., Staveley-Smith, L., et al., 2012, *MNRAS*, 426, 4, 3385, ISSN 0035-8711, <https://academic.oup.com/mnras/article-pdf/426/4/3385/3338965/426-4-3385.pdf>
- Fanaroff, B. L., Riley, J. M., 1974, *MNRAS*, 167, 31P
- Fernández, X., Gim, H. B., van Gorkom, J. H., et al., 2016, *ApJ*, 824, 1, L1, arXiv:1606.00013
- Franzen, T. M. O., Jackson, C. A., Offringa, A. R., et al., 2016, *MNRAS*, 459, 3314, arXiv:1604.03751
- Galassi, M., Davies, J., Theiler, J., et al., 1996, No. Release, 2
- Giovanelli, R., Haynes, M. P., Kent, B. R., et al., 2005, *AJ*, 130, 6, 2598, arXiv:astro-ph/0508301
- Gogate, A. R., Verheijen, M. A. W., van der Hulst, J. M., Jaffé, Y. L., 2023, *MNRAS*, 519, 3, 4279, arXiv:2303.06618
- Gorski, K. M., Hivon, E., Banday, A. J., et al., 2005, *The Astrophysical Journal*, 622, 2, 759
- Guo, H., Jones, M. G., Haynes, M. P., Fu, J., 2020, *ApJ*, 894, 2, 92, arXiv:2004.04762
- Hale, C. L., Jarvis, M. J., Delvecchio, I., et al., 2018, *MNRAS*, 474, 4133, arXiv:1711.05201
- Hamilton, A. J. S., 1993, *ApJ*, 417, 19
- Harris, C. R., Millman, K. J., Van Der Walt, S. J., et al., 2020, *Nature*, 585, 7825, 357
- Hartley, P., Bonaldi, A., Braun, R., et al., 2023, *MNRAS*, arXiv:2303.07943
- Hartley, P., Jackson, N., Sluse, D., Stacey, H. R., Vives-Arias, H., 2019, *MNRAS*, 485, 3, 3009, arXiv:1901.05791
- Haynes, M. P., Giovanelli, R., Kent, B. R., et al., 2018, *ApJ*, 861, 1, 49, arXiv:1805.11499
- Haynes, M. P., Giovanelli, R., Martin, A. M., et al., 2011, *AJ*, 142, 5, 170, arXiv:1109.0027
- Hellwig, H., Vessot, R. F. C., Levine, M. W., Zitzewitz, P. W., Allan, D. W., Glaze, D. J., 1970, *IEEE Transactions on Instrumentation Measurement*, 19, 4, 200
- Holmberg, E., 1958, *Meddelanden fran Lunds Astronomiska Observatorium Serie II*, 136, 1
- Huang, S., Haynes, M. P., Giovanelli, R., Brinchmann, J., 2012, *ApJ*, 756, 2, 113, arXiv:1207.0523
- Ibar, E., Ivison, R. J., Biggs, A. D., Lal, D. V., Best, P. N., Green, D. A., 2009, *MNRAS*, 397, 281, arXiv:0903.3600
- Janssen, R. M. J., Röttgering, H. J. A., Best, P. N., Brinchmann, J., 2012, *A&A*, 541, A62, arXiv:1206.0578
- Jaskot, A. E., Oey, M. S., Salzer, J. J., Van Sistine, A., Bell, E. F., Haynes, M. P., 2015, *ApJ*, 808, 1, 66, arXiv:1506.05081
- Jones, M. G., Haynes, M. P., Giovanelli, R., Moorman, C., 2018, *MNRAS*, 477, 1, 2, arXiv:1802.00053
- Katz, H., Desmond, H., McGaugh, S., Lelli, F., 2019, *MNRAS*, 483, 1, L98, arXiv:1810.12347
- Kellermann, K. I., Condon, J. J., Kimball, A. E., Perley, R. A., Ivezić, Ž., 2016, *ApJ*, 831, 168, arXiv:1608.04586
- Kennicutt, J., Robert C., 1998, *ApJ*, 498, 2, 541, arXiv:astro-ph/9712213
- Kim, H.-S., Wyithe, J. S. B., Baugh, C. M., Lagos, C. d. P., Power, C., Park, J., 2017, *MNRAS*, 465, 1, 111, arXiv:1603.02383
- Koribalski, B. S., Staveley-Smith, L., Westmeier, T., et al., 2020, *Ap&SS*, 365, 7, 118, arXiv:2002.07311
- Kozieł-Wierzbowska, D., Goyal, A., Żywucka, N., 2020, *ApJS*, 247, 2, 53, arXiv:1912.09959
- Landy, S. D., Szalay, A. S., 1993, *ApJ*, 412, 64
- Lin, Y.-T., Shen, Y., Strauss, M. A., Richards, G. T., Lunnan, R., 2010, *ApJ*, 723, 1119, arXiv:1006.5452
- Maddox, N., Frank, B. S., Ponomareva, A. A., et al., 2021, *A&A*, 646, A35, arXiv:2011.09470
- Maddox, N., Hess, K. M., Obreschkow, D., Jarvis, M. J., Blyth, S. L., 2015, *MNRAS*, 447, 2, 1610, arXiv:1412.0852
- Maddox, N., Jarvis, M. J., Oosterloo, T. A., 2016, *MNRAS*, 460, 4, 3419, arXiv:1605.04962
- Magliocchetti, M., Popesso, P., Brusa, M., et al., 2017, *MNRAS*, 464, 3271, arXiv:1606.08286
- Mancuso, C., Lapi, A., Cai, Z.-Y., et al., 2015, *ApJ*, 810, 72, arXiv:1507.08411
- Mancuso, C., Lapi, A., Prandoni, I., et al., 2017, *ApJ*, 842, 95, arXiv:1705.06539
- Mandal, S., Prandoni, I., Hardcastle, M. J., et al., 2021, *A&A*, 648, A5, arXiv:2011.08829
- Martin, A. M., Giovanelli, R., Haynes, M. P., Guzzo, L., 2012, *ApJ*, 750, 1, 38, arXiv:1202.6005
- Massardi, M., Bonaldi, A., Negrello, M., Ricciardi, S., Raccanelli, A., de Zotti, G., 2010, *MNRAS*, 404, 532, arXiv:1001.1069
- Meyer, M., 2009, in *Panoramic Radio Astronomy: Wide-field 1-2 GHz Research on Galaxy Evolution*, 15, arXiv:0912.2167
- Michalowski, M. J., Gentile, G., Hjorth, J., et al., 2015, *A&A*, 582, A78, arXiv:1508.03094
- Naluminsa, E., Elson, E. C., Jarrett, T. H., 2021, *MNRAS*, 502, 4, 5711, arXiv:2101.04514
- Noordermeer, E., van der Hulst, J. M., Sancisi, R., Swaters, R. A., van Albada, T. S., 2005, *A&A*, 442, 1, 137, arXiv:astro-ph/0508319
- Novak, M., Smolčić, V., Delhaize, J., et al., 2017, *A&A*, 602, A5, arXiv:1703.09724
- Obuljen, A., Alonso, D., Villaescusa-Navarro, F., Yoon, I., Jones, M., 2019, *MNRAS*, 486, 4, 5124, arXiv:1805.00934
- Ocran, E. F., Taylor, A. R., Vaccari, M., et al., 2020, *MNRAS*, 491, 4, 5911, arXiv:1912.00934
- Oh, S.-H., Hunter, D. A., Brinks, E., et al., 2015, *AJ*, 149, 6, 180, arXiv:1502.01281
- Oman, K. A., 2022, *MNRAS*, 509, 3, 3268, arXiv:2108.08856
- Padovani, P., Bonzini, M., Kellermann, K. I., Miller, N., Mainieri, V., Tozzi, P., 2015, *MNRAS*, 452, 1263, arXiv:1506.06554
- Papastergis, E., Giovanelli, R., Haynes, M. P., Rodríguez-Puebla, A., Jones, M. G., 2013, *ApJ*, 776, 1, 43, arXiv:1308.2661
- Passmoor, S. S., Cress, C. M., Faltenbacher, A., 2011, *MNRAS*, 412, 1, L50
- Paul, N., Choudhury, T. R., Paranjape, A., 2018, *MNRAS*, 479, 2, 1627, arXiv:1712.04469
- Paul, S., Santos, M. G., Chen, Z., Wolz, L., 2023, arXiv

- e-prints, arXiv:2301.11943, arXiv:2301.11943
- Pedregosa, F., Varoquaux, G., Gramfort, A., et al., 2011, the Journal of machine Learning research, 12, 2825
- Pence, W. D., 2010, Astrophysics Source Code Library, ascl-1010
- Planck Collaboration VI, 2020, A&A, 641, A6, arXiv:1807.06209
- Planck Collaboration XVI, 2014, A&A, 571, A16
- Ponomareva, A. A., Jarvis, M. J., Pan, H., et al., 2023, arXiv e-prints, arXiv:2304.13051, arXiv:2304.13051
- Ponomareva, A. A., Verheijen, M. A. W., Bosma, A., 2016, MNRAS, 463, 4, 4052, arXiv:1609.00378
- Popping, G., Somerville, R. S., Trager, S. C., 2014, MNRAS, 442, 3, 2398, arXiv:1308.6764
- Rajohnson, S. H. A., Frank, B. S., Ponomareva, A. A., et al., 2022, MNRAS, 512, 2, 2697, arXiv:2203.06149
- Rhee, J., Meyer, M., Popping, A., et al., 2023, MNRAS, 518, 3, 4646, arXiv:2210.09697
- Rodríguez, S., Padilla, N. D., 2013, MNRAS, 434, 3, 2153, arXiv:1306.3264
- Siewert, T. M., Hale, C., Bhardwaj, N., et al., 2019, arXiv e-prints, arXiv:1908.10309, arXiv:1908.10309
- Sinigaglia, F., Rodighiero, G., Elson, E., et al., 2022, ApJ, 935, 1, L13, arXiv:2208.01121
- Smith, D. J. B., Haskell, P., Gürkan, G., et al., 2021, A&A, 648, A6, arXiv:2011.08196
- Smolčić, V., Novak, M., Bondi, M., et al., 2017, A&A, 602, A1, arXiv:1703.09713
- Staveley-Smith, L., Oosterloo, T., 2015, in Advancing Astrophysics with the Square Kilometre Array (AASKA14), 167, arXiv:1506.04473
- Swaters, R. A., Sancisi, R., van Albada, T. S., van der Hulst, J. M., 2009, A&A, 493, 3, 871, arXiv:0901.4222
- Swaters, R. A., van Albada, T. S., van der Hulst, J. M., Sancisi, R., 2002, A&A, 390, 829, arXiv:astro-ph/0204525
- The Astropy Collaboration, Robitaille, Thomas P., Tollerud, Erik J., et al., 2013, A&A, 558, A33
- Van Rossum, G., et al., 2007, in USENIX annual technical conference, vol. 41, 1–36, Santa Clara, CA
- Verheijen, M. A. W., Sancisi, R., 2001, A&A, 370, 765, arXiv:astro-ph/0101404
- Vernstrom, T., Scott, D., Wall, J. V., et al., 2016, MNRAS, 462, 2934, arXiv:1603.03085
- Villaescusa-Navarro, F., Genel, S., Castorina, E., et al., 2018, ApJ, 866, 2, 135, arXiv:1804.09180
- Waldram, E. M., Pooley, G. G., Davies, M. L., Grainge, K. J. B., Scott, P. F., 2010, MNRAS, 404, 1005, arXiv:0908.0066
- Walter, F., Carilli, C., Neeleman, M., et al., 2020, ApJ, 902, 2, 111, arXiv:2009.11126
- Wang, J., Fu, J., Aumer, M., et al., 2014, MNRAS, 441, 3, 2159, arXiv:1401.8164
- Wang, J., Koribalski, B. S., Serra, P., et al., 2016, MNRAS, 460, 2, 2143, arXiv:1605.01489
- White, S. V., Jarvis, M. J., Kalfountzou, E., et al., 2017, MNRAS, 468, 217, arXiv:1702.00904
- Whittam, I. H., Riley, J. M., Green, D. A., et al., 2016, MNRAS, 457, 1496, arXiv:1601.00282
- Wong, O. I., Ryan-Weber, E. V., Garcia-Appadoo, D. A., et al., 2006, MNRAS, 371, 4, 1855, arXiv:astro-ph/0607491
- Xi, H., Staveley-Smith, L., For, B.-Q., et al., 2021, MNRAS, 501, 3, 4550, arXiv:2012.09516
- Zhou, Z., Wu, H., Zhou, X., Ma, J., 2018, PASP, 130, 991, 094101, arXiv:1807.09955

APPENDIX A: CONTENT OF THE CATALOGUES

The structure of each T-RECS HI and continuum catalogues is presented in Table A1 and A2, respectively. The continuum catalogues include the AGN and SFG populations. A few of the modelled quantities apply to only one of the populations and are left blank for the other. A flag value of -100 is used in this case.

HI \times continuum catalogues contain all columns in Table A1 and Table A2 with the exception of the second set of coordinates (`x_coord`, `y_coord`, latitude, longitude, redshift) which are rewritten after plausible counterparts between the two catalogues have been identified. Other quantities that have the same name in both catalogues are both kept, and the second set is renamed (e.g. `bmaj_1` instead of `bmaj`). This is because they all contain unique information, (e.g., the size as traced by the stars and by the neutral gas).

APPENDIX B: RUNNING THE COMPLETE T-RECS PIPELINE

Extending T-RECS to include HI and HI-continuum cross-correlation has meant an increase in the code complexity and an evolution in its architecture. Along with these modifications, we have implemented a new build system and a user interface we detail in this appendix.

When building the library, separate FORTRAN modules are compiled, each of which deals with a different modular component of the work-flow. The work-flow is controlled by a master script, accessed as terminal command, which executes calls to the different components. The modules called by the master script are listed below:

- continuum sampler (`trecs_sampler_continuum`) produces a sample of star forming galaxies and AGN to whom a dark mass and a HI mass are associated in order to allow for cross-matching with clustering and HI properties, as detailed in Sec. 3;
- HI sampler (`trecs_sampler_hi`) produces a sample of HI galaxies, with the total HI mass, line width, and morphological properties described in Sec. 2; this catalogue is still un-correlated to the one produced by the continuum module;
- cross-matching of HI properties with continuum properties (`trecs_xmatch_hi`) implements the algorithm matching continuum and HI sources, detailed in Sec. 4. It is used when the outputs of the two modules have to be used as a consistent set on the same sky area. Since the input of this step is given by the HI and continuum catalogues, these are to be computed in advance.
- cross-match of the DM-halo masses with those of the P-Millennium light-cone (Sec. 5) delivered with the input dataset coupled with the library (`trecs_xmatch_clustering`). The coordinates of haloes in the P-Millennium (Baugh et al. 2019) light-cone embed the spatial properties of dark matter

Table A1. Structure of the HI catalogues released with this paper. Catalogues produced with the T-RECS code will have the same format.

Tag Name	Units	Description
ID_HI		Numerical identifier for the source
MHI	$\log(M_{\odot})$	HI mass
HI flux	mJY Hz	HI flux
Mh	$\log(M_{\odot})$	Dark halo mass
Mstar	$\log(M_{\odot})$	Stellar mass
x_coord	degs	First angular coordinate in the flat-sky approximation (see T-RECS I for more details)
y_coord	degs	Second angular coordinate in the flat-sky approximation (see T-RECS I for more details)
latitude	degs	Latitude spherical coordinate for a chosen centre of the field
longitude	degs	Longitude spherical coordinate for a chosen centre of the field
redshift		redshift
HI size	arcsec	Apparent size of the HI source
inclination	degs	galaxy inclination
axis ratio		galaxy axis ratio, defined as the ratio between major and minor axis
bmaj	arcsec	major axis
bmin	arcsec	minor axis
PA	degs	position angle
OptClass		Number identifying the optical type: 1 for elliptical, 2 for spiral

haloes and sub-haloes in a Planck cosmology. If for a source in the T-RECS catalogue a DM-halo counter-part is identified in the light-cone, the sky coordinates of the source are overwritten with those of the associated halo. This cross-match can be applied to each output catalogue of the T-RECS samplers.

- wrapping of the produced catalogues in just one file (`treocs_wrapper`). For parallelisation and RAM-usage purposes, the T-RECS functions are launched and operate on redshift slices that are stored in separate files. The list of redshift slices is reported in table B1. This final module collates the raw outputs into a single catalogue file, rotating the field of view towards user-defined coordinates.

All of the components listed above can be run separately and are independent one from the other with some obvious exceptions (e.g. cross-matching, whether it is between continuum and HI properties or between the sampled catalogues and the DM haloes in the light-cone, requires to have first produced the relevant catalogues to match).

Running the full code requires to provide a parameter file with user-defined properties that will apply to the whole run (e.g. field of view, redshift limits, what output catalogues to cross-match). By changing the initial random seed one can either produce different realisations or reproduce the exact results of some previous run.

As already mentioned, all of the functionalities of the library are wrapped by a command line interface that can be launched by running the

```
$ treocs [OPTIONAL FLAGS]
  -p|--params /path/to/parameter_file.ini
```

command. The optional flags control the overall behaviour and which module(s) to run. An example working call to the command would be:

```
$ treocs --continuum --HI
  --xmatch --clustering
  --wrap HI_continuum
  --params /path/to/parameter_file.ini
```

the command executes continuum sampling and HI sampling then it cross-matches the two catalogues and assigns coordinates in the light-cone to as many sources as possible; finally, the raw catalogues are wrapped into one single file with sky coordinates rotated to match the user-defined field of view.

Tab. B2 summarizes the available command line options and the different types of simulations that are generated by calling the `treocs` command with different combinations of arguments. A manual page with an explanation of all available optional flags is shown on screen by calling the `treocs` command with the `-h|--help` flag.

This paper has been typeset from a $\text{\TeX}/\text{\LaTeX}$ file prepared by the author.

Table A2. Structure of the radio continuum catalogues released with this paper. Catalogues produced with the T-RECS code will have the same format except for the number and list of frequencies and the possibility to optionally output the luminosities for each frequency as additional columns.

Tag Name	Units	Description
ID_cont		Numerical identifier for the source
Lum ₁₄₀₀	log(erg/s/Hz)	Luminosity at 1.4 GHz (AGN only)
logSFR	log(M_{sun})/yr	SFR (SFG only)
I _{freq}	mJy	Total intensity flux density of the source at frequency <i>freq</i> for each of a list of N_{freqs} frequencies as specified by the user.
P _{freq}	mJy	Polarized flux density of the source at frequency <i>freq</i> for each of a list of N_{freqs} frequencies as specified by the user. See T-RECS I for details of the polarization model.
Mh	log(M_{sun})	Dark halo mass
Mstar	log(M_{sun})	Stellar mass
MHI_pred	log(M_{sun})	HI mass proxy
x_coord	degs	First angular coordinate in the flat-sky approximation (see T-RECS I for more details)
y_coord	degs	Second angular coordinate in the flat-sky approximation (see T-RECS I for more details)
latitude	degs	Latitude spherical coordinate for a chosen centre of the field
longitude	degs	Longitude spherical coordinate for a chosen centre of the field
redshift		redshift
size	arcsec	Apparent size of the source. This is the maximum size of the core+jet emission for AGN, and the scale radius of a Sersic profile for SFG.
inclination	degs	galaxy inclination
axis_ratio		galaxy axis ratio, defined as the ratio between major and minor axis
bmaj	arcsec	major axis
bmin	arcsec	minor axis
PA	degs	position angle
Rs		Ratio between the distance between the spots and the total size of the jets, for the FR I /FR II classification (steep-spectrum AGN only)
RadioClass		Number identifying the sub-population: 1 for late-type; 2 for spheroids; 3 for lensed spheroids; 4 for FSRQ, 5 for BL Lac and 6 for SS-AGN.
OptClass		Number identifying the optical type: 1 for elliptical, 2 for spiral.
L _{freq}	erg/s/Hz	OPTIONAL OUTPUT: Luminosity of the source at frequency <i>freq</i> for each of a list of N_{freqs} frequencies as specified by the user.

Table B1. Redshift slices adopted in T-RECS

Central z	Minimum z	Maximum z
0.01	0.00	0.01
0.02	0.01	0.03
0.05	0.03	0.07
0.10	0.07	0.12
0.15	0.12	0.17
0.20	0.17	0.22
0.25	0.22	0.27
0.30	0.27	0.32
0.35	0.32	0.37
0.40	0.37	0.42
0.45	0.42	0.47
0.50	0.47	0.52
0.55	0.52	0.57
0.60	0.57	0.62
0.65	0.62	0.67
0.70	0.67	0.72
0.75	0.72	0.77
0.80	0.77	0.82
0.85	0.82	0.87
0.90	0.87	0.92
0.95	0.92	0.97
1.00	0.97	1.10
1.20	1.10	1.30
1.40	1.30	1.50
1.60	1.50	1.70
1.80	1.70	1.90
2.00	1.90	2.10
2.20	2.10	2.30
2.40	2.30	2.50
2.60	2.50	2.70
2.80	2.70	2.90
3.00	2.90	3.10
3.20	3.10	3.30
3.40	3.30	3.50
3.60	3.50	3.70
3.80	3.70	3.90
4.00	3.90	4.10
4.20	4.10	4.30
4.40	4.30	4.50
4.60	4.50	4.70
4.80	4.70	4.90
5.00	4.90	5.10
5.20	5.10	5.30
5.40	5.30	5.50
5.60	5.50	5.70
5.80	5.70	5.90
6.00	5.90	6.10
6.20	6.10	6.30
6.40	6.30	6.50
6.60	6.50	6.70
6.80	6.70	6.90
7.00	6.90	7.10
7.20	7.10	7.30
7.40	7.30	7.50
7.60	7.50	7.70
7.80	7.70	7.90
8.00	7.90	8.10

Table B2. Optional flags of the T-RECS terminal command (`trecs`) and the different type of simulation they produce if added. The [TAG] argument in the last column determines which raw catalogue to wrap (e.g. HI for the output of the HI sampler, HI.continuum for the cross-matched catalogue). The pipe symbol (|) in the column labels specifies that the flag can be called in two equivalent ways.

Simulation type	--HI -i	--continuum -c	--xmatch -x	--clustering -C	--wrap -w [TAG]
HI, no clustering	X				HI
HI, with clustering	X			X	HI_clustering
Continuum, no clustering		X			continuum
Continuum, with clustering		X		X	continuum_clustering
Continuum \times HI, no clustering	X	X	X		HI_continuum
Continuum \times HI, with clustering	X	X	X	X	HI_continuum_clustering